RESEARCH ARTICLE

Check for updates

Temperature- and solvent-induced reversible single-crystal-to-single-crystal transformations of Tb[III]-based MOFs with excellent stabilities and fluorescence sensing properties toward drug molecules†

Yu Li,‡ Bi-Lian Chai,‡ Hui Xu, Teng-Fei Zheng, [ID] Jing-Lin Chen, [ID] Sui-Jun Liu [ID] * and He-Rui Wen [ID]

Recently, single-crystal-to-single-crystal conversion has been a hot topic in the field of metal–organic framework (MOF) materials, which could improve the stability and properties due to structural changes. A new Tb[III]-based MOF ([Tb$_4$(BTDI)$_3$(DMF)$_4$]$_n$, **JXUST-12**) has been designed and synthesized by the incorporation of Tb[III] ions and H$_4$BTDI ligands (5,5′-(benzo[c][1,2,5]thiadiazole-4,7-diyl)diisophthalic acid) featuring a fluorescent unit. Very interestingly, the reversible single-crystal-to-single-crystal transformation between **JXUST-12** and {[Tb$_4$(BTDI)$_3$(H$_2$O)$_4$]·4H$_2$O·solvents}$_n$ (**JXUST-12a**) occurred, and thus the enhancement of water and pH stabilities has been achieved. Because of the presence of Tb[III] ions and the fluorescent organic ligand, **JXUST-12** and **JXUST-12a** can be used as luminescent sensors for the detection of drugs (NFT = nitrofurantoin, NZF = nitrofurazone, and DCN = 2,6-dichloro-4-nitroaniline). Furthermore, theoretical caculations and experimental studies suggest that the luminescence quenching of **JXUST-12** and **JXUST-12a** for the detection of NFT, NZF and DCN may be attributed to a competitive energy absorption and photoinduced electron transfer mechanism. Remarkably, fluorescent test papers and composite films based on **JXUST-12** and **JXUST-12a** have been developed to simply detect drugs through the visual change of the luminescence colour.

Introduction

Metal–organic frameworks (MOFs) have potential application prospects in the fields of sensing,[1,2] catalysis,[3] magnetism,[4] proton conduction[5] and gas adsorption and separation[6,7] due to the abundant topological networks,[8] high specific surface area[9] and adjustable optical properties.[10] Single-crystal-to-single-crystal (SCSC) conversion is an effective way to reconstruct the structures of MOFs[11] accompanied by the changes

School of Chemistry and Chemical Engineering, Jiangxi Provincial Key Laboratory of Functional Molecular Materials Chemistry, Jiangxi University of Science and Technology, Ganzhou 341000, Jiangxi Province, P.R. China.
E-mail: sjliu@jxust.edu.cn; Tel: +86-797-8312204

†Electronic supplementary information (ESI) available: X-ray crystallographic data, selected bond lengths and angles, SHAPE analysis of the Tb[III] ions, ESI table, structural figures, part of the experimental details, IR, PXRD, TGA curves, luminescence spectra and UV-vis absorption spectra. CCDC 2126107 (**JXUST-12**) and 2126108 (**JXUST-12a**). For ESI and crystallographic data in CIF or other electronic format see DOI: 10.1039/d2qi00023g

‡These authors contributed equally to this work and should be considered co-first authors.

of coordination bonds, dimensions and porosity.[12–15] Interestingly, SCSC conversion can improve the stability[16,17] and luminescence performance[18] of MOFs. Luminescent metal–organic frameworks (LMOFs) have been proven to be one of the most promising luminescence sensing materials because of the expected luminescence features.[1,19–21] In addition, the aqueous stability of LMOFs is important for exploring their sensing properties.[17]

Drugs have brought us great advantages in the prevention and treatment of human, animal and plant infectious diseases, but the abuse of drugs can cause harm to the environment and human health.[22–26] For example, nitrofuran drugs including nitrofurantoin (NFT) and nitrofurazone (NZF), and 2,6-dichloro-4-nitroaniline (DCN) in organochlorine pesticides are highly toxic and non-degradable, increasing the risk of human cell mutation and carcinogenicity.[27–30] In addition, ofloxacin (OFX) and fleroxacin (FO) in fluoroquinolone drugs can affect the stomach, skin and central nervous system of the human body.[31–33] The traditional detection methods (high performance liquid chromatography-mass spectrometry and spectrophotometry) are complicated and of high cost.[22,34,35]

1504 | *Inorg. Chem. Front.*, 2022, **9**, 1504–1513

This journal is © the Partner Organisations 2022

Therefore, there is an urgent need for simple, rapid and efficient detection of the drugs. LMOF sensing can be used as a method to detect drugs due to their advantages in terms of definite fluorescence spectra, visible signals by the naked eye, high sensitivity and selectivity, and simplicity in operation.[36–38]

2,1,3-Benzothiadiazole (BTD) is a chromophore and an electron withdrawing group, with rich photophysical and photochemical properties, and its derivatives have broad prospects in the field of molecular luminescent probes.[39–42] Herein, 5,5′-(benzo[c][1,2,5]thiadiazole-4,7-diyl)diisophthalic acid (H_4BTDI) was chosen as the primary ligand and a three-dimensional (3D) Tb^{III}-based MOF ($\{[Tb_4(BTDI)_3(H_2O)_4]\cdot4H_2O\cdot solvents\}_n$, **JXUST-12a**) was obtained by the reversible conversion of $[Tb_4(BTDI)_3(DMF)_4]_n$ (**JXUST-12**) under the heating conditions of 410 °C. In this work, the enhancement of water stability of the LMOF has been achieved by the SCSC transformation and the reversible conversion of the LMOF makes it more convenient and less expensive to sense harmful substances. **JXUST-12** and **JXUST-12a** were used as luminescent probes to detect drug molecules. Notably, **JXUST-12a** exhibits excellent water and pH stabilities as well as fluorescence sensing properties toward NFT, NZF, DCN, OFX and FO. The limits of detection (LODs) of **JXUST-12a** for the detection of NFT and NZF are lower than that of **JXUST-12**. In addition, the sensing mechanisms of **JXUST-12** and **JXUST-12a** were also investigated in detail.

Experimental section

Synthesis of $[Tb_4(BTDI)_3(DMF)_4]_n$ (JXUST-12)

JXUST-12 was solvothermally synthesized based on a mixture of $Tb(NO_3)_3\cdot6H_2O$ (22.7 mg, 0.05 mmol), H_4BTDI (11.6 mg, 0.025 mmol), 4,4′-bipyridine (15.6 mg, 0.1 mmol), N,N'-dimethylformamide (DMF, 7 mL), formic acid (500 μL) and water (3 mL). The mixture was stirred for 30 minutes and put into a 25 mL Teflon-lined autoclave, which was heated to 160 °C for 72 h. After cooling to room temperature, yellow block crystals were collected with 65.71% yield based on H_4BTDI. Elemental analysis (%) calcd for $C_{78}H_{52}N_{10}S_3Tb_4O_{28}$: C, 40.57; H, 2.27; N, 6.07; S, 4.17. Found: C, 39.85; H, 2.38; N, 5.69; S, 3.81. IR (KBr, cm^{-1}): 3061w, 1662s, 1617s, 1534s, 1447s, 1395s, 1114w, 845m, 782m, 754m, 713m, 674w, 529w, 434w (Fig. S2, ESI†).

Reversible transformations between JXUST-12 and $\{[Tb_4(BTDI)_3(H_2O)_4]\cdot4H_2O\cdot solvents\}_n$ (JXUST-12a)

When the TG-DTA analyzer was heated at 410 °C for 15 minutes, **JXUST-12** transformed to **JXUST-12a** by replacing two coordinated DMF molecules with two water molecules without losing crystallinity. Remarkably, the block crystals of **JXUST-12a** could gradually change to **JXUST-12′** (the same structure of **JXUST-12**) without losing crystallinity when **JXUST-12a** was heated at 160 °C to reflux in 10 mL DMF solution for 3 days (Fig. 1). Elemental analysis (%) calcd for $C_{78}H_{52}N_{10}S_3Tb_4O_{28}$: C, 37.31; H, 1.71; N, 3.96; S, 4.53. Found:
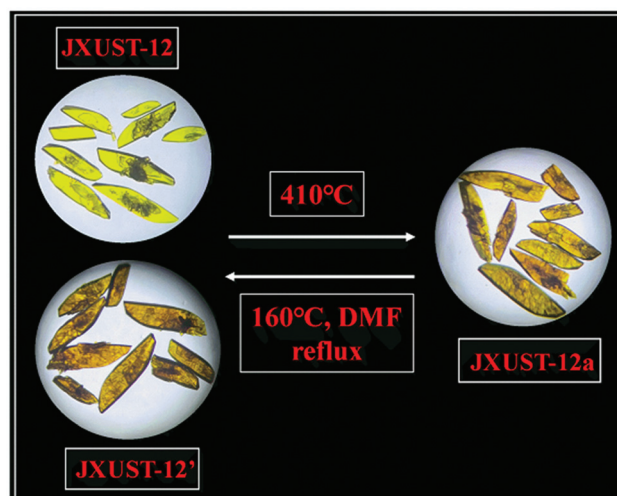

Fig. 1 Photographs of the reversible transformations between **JXUST-12** and **JXUST-12a** in natural light.

C, 35.11; H, 2.42; N, 4.01; S, 4.56. IR (KBr pellets, cm^{-1}): 3612w, 3420w, 3063w, 1640s, 1530s, 1451s, 1397s, 1118w, 853w, 757m, 715m, 533w, 437w (Fig. S2, ESI†).

Results and discussion

Structural description of JXUST-12 and JXUST-12a

Single-crystal X-ray diffraction studies suggest that **JXUST-12** and **JXUST-12a** crystallize in the triclinic system with the $P\bar{1}$ space group. The asymmetric unit of **JXUST-12** contains two crystallographically independent Tb^{III} ions, one and a half $BTDI^{4-}$ ligands and two DMF molecules (Fig. 2a). The asymmetric unit of **JXUST-12a** is similar to that of **JXUST-12** except for two coordinated and two lattice H_2O molecules (Fig. 2b). In **JXUST-12**, seven-coordinate Tb1 and Tb2 present a capped trigonal prism coordination configuration calculated using the SHAPE 2.1[43] software (Table S4 and Fig. S1c, ESI†). The coordination configuration of Tb2 in **JXUST-12a** is the same as that of Tb2 in **JXUST-12** (Table S5 and Fig. S1d, ESI†), while the coordination configuration of eight-coordinate Tb1 in **JXUST-12a** is square antiprism (Table S5 and Fig. S1d, ESI†). The coordination modes of carboxylate groups in **JXUST-12** are $syn–syn$-μ_2-η^1:η^1, syn-$anti$-μ_2-η^1:η^1 and μ-η^1:η^1 (Fig. S1a, ESI†), while the coordination modes of carboxylate groups in **JXUST-12a** are similar to those of **JXUST-12** except that $syn–anti$-μ_2-η^1:η^1 is replaced by $syn–anti$-μ_2-η^1:η^2 (Fig. S1b, ESI†). As shown in Fig. 2a and b, Tb1 of **JXUST-12** and **JXUST-12a** is surrounded by six or seven O atoms from the carboxylate groups of five different $BTDI^{4-}$ ligands and one O atom from DMF or H_2O, while Tb2 is coordinated with six O atoms from five distinct $BTDI^{4-}$ ligands and one O atom from DMF or H_2O. The adjacent Tb1 and Tb2 are bridged by carboxylate O atoms from $BTDI^{4-}$ ligands to constitute a $[Tb_2(COO)_2]$ secondary building unit, which is further linked by $BTDI^{4-}$ ligands to form a three-dimensional structure (Fig. 2c and d).
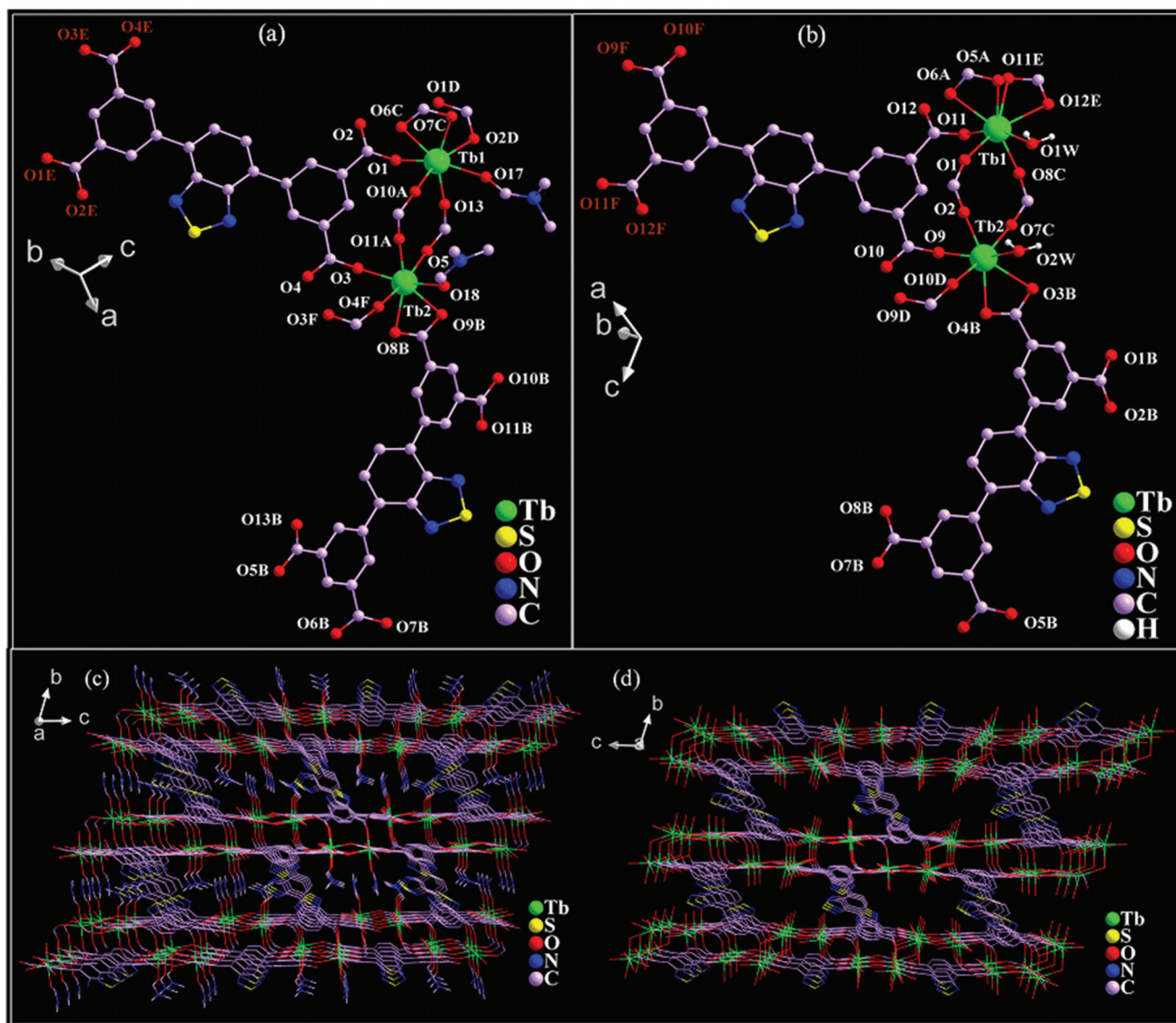
Fig. 2 (a) Ball-and-stick view of the coordination environments of Tb^{III} in **JXUST-12** (symmetry codes: A, $x, y, z − 1$; B, $x + 1, y, z − 1$; C, $x − 1, y, z$; D, $−x, −y + 1, −z + 1$; E, $−x + 1, −y + 1, −z$). (b) Ball-and-stick view of the coordination environments of Tb^{III} in **JXUST-12a** (symmetry codes: A, $x, y, z − 1$; B, $x − 1, y, z$; C, $x − 1, y, z − 1$; D, $−x, −y + 1, −z$; E, $−x, −y + 1, −z − 1$; F, $−x + 1, −y + 2, −z$). (c) The 3D structure of **JXUST-12**. (d) The 3D structure of **JXUST-12a**.

Stability of JXUST-12 and JXUST-12a

As presented in Fig. S3a and S3c (ESI†), the peaks in the PXRD patterns of the as-synthesized samples of **JXUST-12** and **JXUST-12a** are in good agreement with the simulated ones. Both **JXUST-12** and **JXUST-12a** exhibit excellent solvent stability toward common solvents (Fig. S3b and S3d, ESI†). Notably, **JXUST-12a** exhibits excellent water and pH stabilities (Fig. S3c and S3e, ESI†). When the crystal sample of **JXUST-12a** was immersed in water at room temperature for a week and stored in boiling water for 24 h, the framework still remained stable. The PXRD patterns of **JXUST-12a** after soaking in aqueous solutions with pH values of 1–12 are in good agreement with the simulated one, indicating that **JXUST-12a** has excellent pH

stability. The size and morphology of **JXUST-12** and **JXUST-12a** were characterized by the scanning electron microscopy method (Fig. S5, ESI†). The results show a rectangular block structure with an average particle size of 0.32 mm and 0.23 mm for **JXUST-12** and **JXUST-12a**, respectively.

TGA was performed from room temperature to 900 °C (or 1000 °C) under a N$_2$ atmosphere to explore the thermal stabilities of **JXUST-12** and **JXUST-12a**. As displayed in Fig. S4a (ESI†), **JXUST-12** remained stable before 285 °C, and the weight loss of 13.8% between 285 °C and 540 °C was due to the loss of the coordinated DMF molecules. Subsequently, the framework began to collapse after 540 °C, demonstrating that **JXUST-12** displayed a relatively good thermal stability. Similarly, the mass loss of 13.6% for **JXUST-12a** was due to the

removal of free H_2O molecules in the channel and coordination of H_2O molecules before reaching 540 °C (Fig. S4b, ESI†).

Fluorescence behaviors

Generally, MOFs constructed by rare earth ions and conjugated BTD-based organic ligands can display excellent luminescence properties.[1,11,44] The emission spectra of H_4BTDI, **JXUST-12** and **JXUST-12a** were investigated in the solid state at room temperature. As shown in Fig. S6a (ESI†), the emission peaks of H_4BTDI ligand, **JXUST-12** and **JXUST-12a** occurred at 515, 510 and 520 nm upon excitation at 370 nm, respectively. The emission of H_4BTDI ligand might be ascribed to the intraligand $\pi^\star \rightarrow \pi$ or $\pi^\star \rightarrow n$ transitions.[45] In addition, **JXUST-12** and **JXUST-12a** exhibited emission peaks at 499 and 504 nm in EtOH solution, respectively. The quantum efficiencies of **JXUST-12** and **JXUST-12a** are 16.07% and 1.93%, respectively. The emission peaks at 505 nm in aqueous solution were observed for **JXUST-12a** (Fig. S6b, ESI†). The emission peaks of **JXUST-12** and **JXUST-12a** in solvents were different from those in the solid state, which was influenced by the solvent effect.

Selective sensing of drug molecules

The luminescence performance of **JXUST-12** and **JXUST-12a** prompted us to investigate the sensing properties toward drugs for antibiotics (NFT, NZF, FO, OFX, ornidazole (ODZ), metronidazole (MDZ), sulfamethazine (SMZ), sulfadiazine (SDZ), florfenicol (FFC), chloramphenicol (CAP) and 3-nitropropionic (3-NPA)) and non-antibiotics (DCN and 4-nitroimidazole (4-ND)). All fluorescence experiments were performed at room temperature. The stable suspension was prepared by immersing 0.5 mg finely ground sample in 2 mL dispersant and sonicating for 30 minutes.

The samples of **JXUST-12a** were dispersed in EtOH or aqueous solutions (2 mL) containing 5 μL different drug molecules (0.2 M) to conduct luminescence experiments. Different from **JXUST-12a**, the fluorescence experiment of **JXUST-12** was carried out in EtOH solution. The results show that **JXUST-12** has a turn-off effect on NFT, NZF and DCN, and the luminescence quenching efficiencies (Q) reached 99.53%, 99.62% and 99.45%, respectively (Fig. 3). Q is calculated using the following formula: $Q = (I_0 - I)/I_0 \times 100\%$ (I_0 and I are the maximum luminescence intensities before and after the addition of the target analyte).[46] Therefore, **JXUST-12** can be considered as a promising luminescent probe for NFT, NZF and DCN molecules. Furthermore, anti-interference experiments were performed to validate the high selectivity of **JXUST-12** for the detection of NFT, NZF and DCN. By mixing NFT, NZF and DCN with various coexisting drugs, respectively (the ratio of NFT/NZF/DCN and coexisting drugs was 1 : 1), the luminescence turn-off effect was still retained (Fig. S12, ESI†), implying that **JXUST-12** could selectively detect NFT, NZF and DCN in the presence of other drugs. To better investigate the sensitivity of **JXUST-12** towards NFT, NZF and DCN, titration experiments with varying concentrations of NFT, NZF and
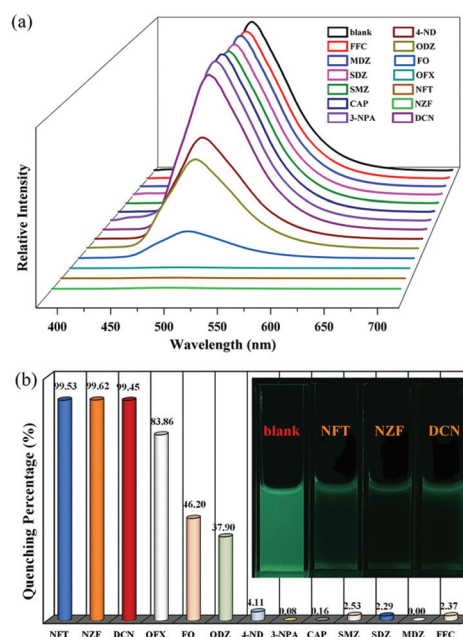

Fig. 3 (a) The emission spectra of **JXUST-12** dispersed in EtOH solution containing different drug molecules. (b) The quenching efficiencies of **JXUST-12** dispersed in the EtOH solution containing different drug molecules (inset: the photographs of **JXUST-12** dispersed in EtOH solutions containing NFT, NZF and DCN under a 365 nm UV-lamp).

DCN were also performed through gradually adding NFT, NZF and DCN (0.004 M) to the suspension of **JXUST-12**. The intensity of **JXUST-12** gradually decreased upon the addition of NFT, NZF and DCN (Fig. 5). The fitted Stern–Volmer (SV) curves showed that there was a good linear relationship between luminescence intensities and the concentrations of NFT, NZF and DCN (Fig. S7, ESI†). According to the Stern–Volmer equation: $I_0/I = 1 + K_{SV}[M]$,[47] the K_{SV} values of NFT, NZF and DCN are 4.36×10^4 M^{-1}, 4.33×10^4 M^{-1} and 4.75×10^4 M^{-1}, respectively ([M] is the concentration of NFT, NZF and DCN; I_0 and I are the luminescence intensities of **JXUST-12** before and after adding analytes; and K_{SV} is the quenching coefficient (M^{-1})). The LODs calculated using the $3\sigma/k$ formula (σ: standard error and k: the slope)[48] for NFT, NZF and DCN are 0.86, 0.82 and 0.88 μM, respectively (Fig. 5 and S7, ESI†). As shown in Table S6 (ESI†), NFT, NZF and DCN identified by **JXUST-12** have higher K_{SV} values and lower LODs, so **JXUST-12** could be used as a potential candidate for selective detection of NFT, NZF and DCN with high selectively and sensitivity. Considering the cost of materials synthesis, the reusable performance plays an important role in luminescent probes and thus the cyclic experiment was performed. The Q of **JXUST-12** was retained even after 5 cycles (Fig. S16a, ESI†), and could be reused by washing with EtOH several times. The PXRD patterns of the fifth recycled samples were consistent with the simulated one (Fig. S17a, ESI†), indicating that the framework still remained stable. These results reveal that **JXUST-12** has high selectivity, sensitivity and recyclability toward NFT, NZF and DCN.

This journal is © the Partner Organisations 2022

Inorg. Chem. Front., 2022, **9**, 1504–1513 | **1507**

Similarly, **JXUST-12a** also exhibited a turn-off effect for detecting NFT, NZF and DCN in EtOH solution (Fig. S8a, ESI†). A series of fluorescence experiments for sensing NFT, NZF and DCN were performed, which demonstrated that **JXUST-12a** had good anti-interference ability and recyclability (Fig. S13, S16b and S17b, ESI†). The Q value reached 99.34% (NFT), 99.21% (NZF) and 99.81% (DCN), respectively (Fig. S8b, ESI†). The K_{sv} values of NFT, NZF and DCN are 4.36×10^4 M^{-1}, 4.33×10^4 M^{-1} and 4.75×10^4 M^{-1}, respectively (Table S6, ESI†). The LODs of **JXUST-12a** sensing for NFT, NZF and DCN were calculated to be 0.44, 0.40 and 0.34 μM, respectively (Fig. S9, ESI†), which were lower than those of **JXUST-12** and other reported examples (Table S6, ESI†).

Due to the excellent water stability, **JXUST-12a** was used to sense drug molecules in the aqueous solution. The results showed that **JXUST-12a** exhibited a fluorescence turn-off effect toward NFT and NZF, and a fluorescence turn-on effect and blue shift of emission peaks toward OFX and FO (Fig. 4a). The fluorescence effects of **JXUST-12a** and **JXUST-12a** containing OFX and FO were obvious in the CIE chromaticity diagram (Fig. S11, ESI†). The Q value reached 99.34% (NFT) and 99.32% (NZF), respectively (Fig. 4b). According to the fluorescence enhancement equation: $I/I_0 = 1 + K_{ec}[M]$[49] (K_{ec} is the enhancement coefficient (M^{-1})), the K_{sv}/K_{ec} values of NFT, NZF, OFX and FO are 1.74×10^5 M^{-1}, 1.43×10^5 M^{-1}, 5.11×10^3 M^{-1} and 6.03×10^3 M^{-1}, respectively (Table S6, ESI†). The LODs of **JXUST-12a** toward NFT, NZF, OFX and FO were 0.39, 0.43, 7.34 and 2.28 μM, respectively (Fig. 6 and S10, ESI†).
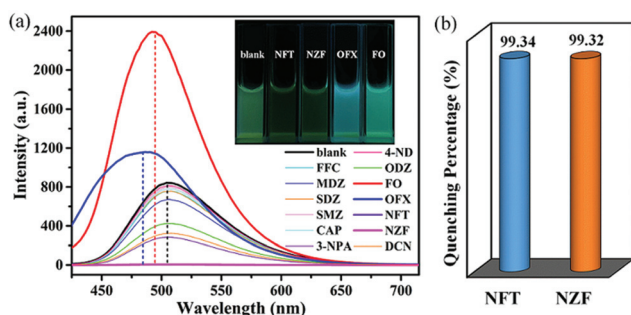

Fig. 4 (a) Emission spectra of **JXUST-12a** dispersed in aqueous solutions containing different drug molecules. (b) Quenching efficiencies of NFT and NZF containing **JXUST-12a** dispersed in the aqueous solution.

NFT, NZF, OFX and FO identified by **JXUST-12a** had higher K_{sv}/K_{ec} values, lower LODs and a better recognition effect than some reported examples (Table S6, ESI†). As shown in Fig. S14, S16c and S17c (ESI†), **JXUST-12a** had high anti-interference ability and recyclability toward NFT and NZF. Additionally, the time responses of **JXUST-12a** for detecting OFX and FO were determined and the luminescence intensities of **JXUST-12a** were continuously recorded with the addition of 5 μL of 0.2 M OFX and FO in aqueous solution. The emission peak shifted gradually and accompanied by increasing fluorescence intensity (Fig. S15, ESI†), which showed the highly effective sensing process for OFX and FO. The results showed that **JXUST-12a** could be considered as an excellent luminescent sensor for detecting NFT, NZF, OFX and FO in aqueous solutions.

It is significant for luminescent materials to be used as devices for practical applications. For providing simple and handy detection, fluorescent test papers and composite films were further developed. The sample and filter paper were soaked in EtOH solutions and ultrasonicated for 30 minutes to form fluorescent test papers. The composite film materials were attained by adding poly(methyl methacrylate) (PMMA) and **JXUST-12** or **JXUST-12a** in DMF, and then heating at 35 °C. Then fluorescent test papers and composite films were used to detect the analytes. As shown in Fig. 7 and 8, the fluorescence test papers and composite films of **JXUST-12** and **JXUST-12a** had significant color changes observed with the naked eye under a 365 nm UV lamp before and after adding NFT, NZF, DCN, OFX or FO. The composite films of **JXUST-12** and **JXUST-12a** have excellent flexibility (Fig. 8a and d). Therefore, the fluorescence test papers and composite films of **JXUST-12** and **JXUST-12a** could be used as simple and handy luminescent probes.[50]

Detection mechanism

The related mechanisms of detecting analytes have been discussed. Generally, the luminescence change induced by small molecules may be attributed to the following mechanisms: (1) structure collapse,[51] (2) competitive energy absorption,[29] (3) absorbance caused enhancement (ACE),[49] and (4) photo-induced electron transfer (PET).[52,55] Herein, in order to confirm the mechanism of luminescence quenching of **JXUST-12** and **JXUST-12a** toward NFT, NZF and DCN in EtOH
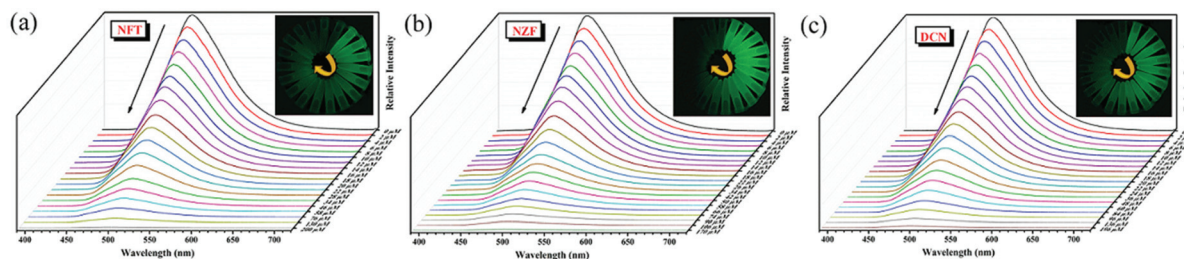

Fig. 5 Emission spectra of **JXUST-12** dispersed in EtOH solutions with various concentrations of NFT (a), NZF (b) and DCN (c). (Inset: photographs of **JXUST-12** with NFT (a, 0–200 μM), NZF (b, 0–170 μM) and DCN (c, 0–196 μM) under a 365 nm UV-lamp.)
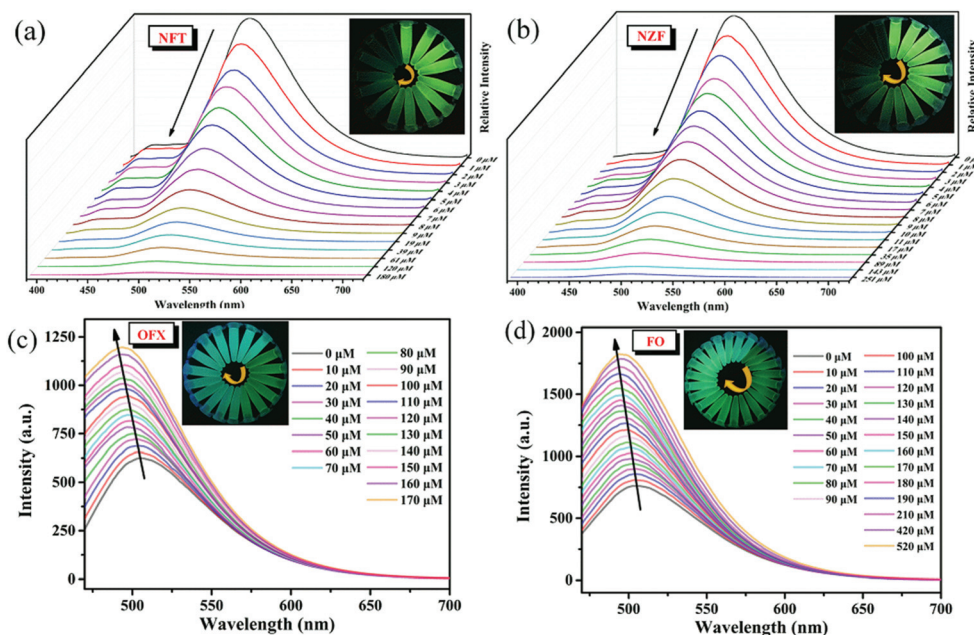
1508 | *Inorg. Chem. Front.*, 2022, **9**, 1504–1513

This journal is © the Partner Organisations 2022

Fig. 6 Emission spectra of **JXUST-12a** dispersed in aqueous solutions with various concentrations of NFT (a), NZF (b), OFX (c) and FO (d). (Inset: photographs of **JXUST-12a** with NFT (a, 0–180 μM), NZF (b, 0–251 μM), OFX (c, 0–170 μM) and FO (d, 0–520 μM) under a 365 nm UV-lamp.)
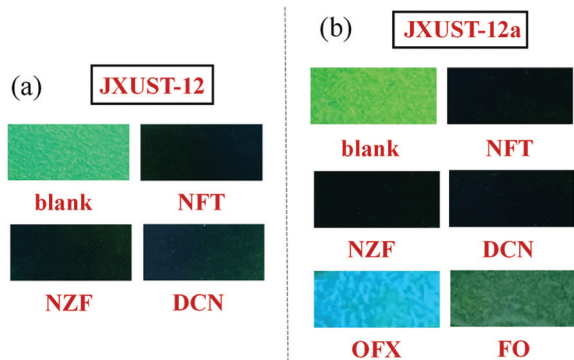

Fig. 7 Optical images of **JXUST-12** (a) and **JXUST-12a** (b) based fluorescent test papers with various drugs under 365 nm UV light.
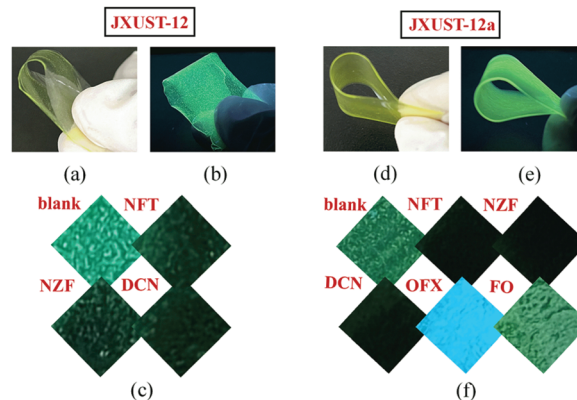

Fig. 8 Optical images of **JXUST-12** and **JXUST-12a** based composite films with various drug molecules in natural light (a and d) and under a 365 nm UV-lamp (b, c, e and f).

solution, the stability of **JXUST-12** and **JXUST-12a** before and after adding NFT, NZF and DCN molecules was respectively explored. The PXRD patterns of **JXUST-12** and **JXUST-12a** dispersed in EtOH solutions of NFT, NZF and DCN were very well consistent with the simulated ones (Fig. S18a, ESI†), demonstrating that the mechanism of the collapse of the framework could be excluded. Then, the UV-vis absorption spectra of **JXUST-12** and **JXUST-12a** upon the addition of NFT, NZF or DCN in EtOH solution were measured. The UV-vis absorption spectra of NFT, NZF and DCN in the range of 335 to 385 nm were basically overlapped with the fluorescence excitation spectra of **JXUST-12** and **JXUST-12a**, while no obvious peaks were observed for other drug molecules in the same wavelength range (Fig. S19a, ESI†). The results demonstrated that the competitive absorption between NFT (or NZF and DCN)

and the excitation of **JXUST-12** and **JXUST-12a** led to fluorescence quenching.[29,52] Besides, PET is a process of excited electron transfer from the photo-excited donor (luminophores) to the lowest unoccupied molecular orbital (LUMO) of the acceptor.[53] The main driving force is the energy gap between the LUMO of the reactants.[54] NFT, NZF and DCN with strong electron withdrawing groups (–NO$_2$) and the LUMO might have caused excitation of electrons from the conduction band of the excited states of **JXUST-12** and **JXUST-12a**.[55] Therefore, the luminescence quenching of **JXUST-12** and **JXUST-12a** toward NFT, NZF and DCN in the EtOH solution might be attributed to the PET mechanism. Because the luminescence of **JXUST-12** mainly originated from H$_4$BTDI ligand, the PET

This journal is © the Partner Organisations 2022

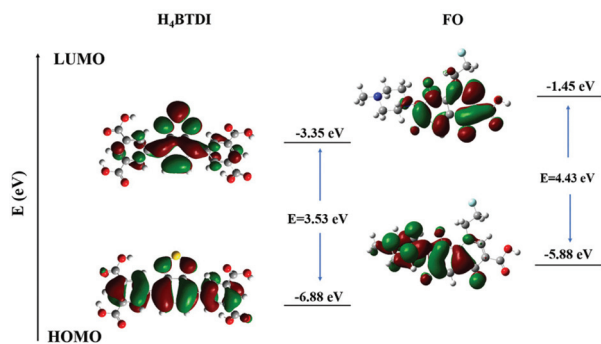*Inorg. Chem. Front.*, 2022, **9**, 1504–1513 | **1509**

Fig. 9 The calculated contour plots of the HOMO, LUMO and HOMO–LUMO energy band gaps for H₄BTDI and FO.

process between the H₄BTDI ligand and NFT (or NZF, DCN) might quench the luminescence of **JXUST-12**. To further demonstrate the PET mechanism, the calculation based on density functional theory (DFT) was implemented. The LUMO energy level of H₄BTDI (−3.35 eV) (Fig. 9) was higher than those of NFT (−3.86 eV) and NZF (−3.62 eV),[33] which supported the PET process from H₄BTDI to NFT and NZF. However, the LUMO energy level of H₄BTDI (−3.35 eV) was lower than that of DCN (−2.4 eV),[30] which was not supported by the PET process from H₄BTDI to DCN. Therefore, the mechanism of the luminescence quenching for **JXUST-12** and **JXUST-12a** on adding NFT and NZF in the EtOH solution might be due to the competitive energy absorption mechanism and the PET mechanism, while the quenching of **JXUST-12** and **JXUST-12a** induced by DCN was due to the existence of competitive absorption.

The mechanisms of **JXUST-12a** sensing NFT, NZF, OFX and FO in the aqueous solution were also studied. Because **JXUST-12a** had the same quenching effect after adding NFT and NZF in the EtOH and aqueous solutions, it can be speculated that they could have the same quenching mechanism. Firstly, the luminescence quenching did not stem from the collapse of the framework because of the structural integrity of the recyclable sample confirmed by the PXRD patterns (Fig. S18c, ESI†). Secondly, the absorption spectra of the NFT and NZF in aqueous solutions were overlapped with the excitation spectra of **JXUST-12a** (Fig. S19b, ESI†). Thirdly, the PET process from H₄BTDI to NFT and NZF is confirmed because the LUMO energy level of H₄BTDI was higher than those of NFT and NZF. Similar to **JXUST-12a** in the EtOH solution, the fluorescence quenching of **JXUST-12a** in the aqueous solution toward NFT and NZF might be due to the competitive energy absorption and PET mechanism.

In addition, the mechanisms of fluorescence enhancement and blue shift of **JXUST-12a** on adding OFX and FO in the aqueous solution were explored. The PXRD patterns of **JXUST-12a** before and after adding OFX and FO matched well with the simulated one, indicating the retention of the framework (Fig. S18c, ESI†). The UV-vis absorption spectra of **JXUST-12a** on adding OFX and FO was measured. The results

showed that the absorbance increased significantly from 250 to 400 nm after the addition of OFX and FO (Fig. S20, ESI†). At the same time, the absorbance gradually enhanced with the increase of the concentration of OFX and FO (Fig. S21, ESI†), indicating that the fluorescence turn-on effect and blue shift of **JXUST-12a** on adding OFX and FO in the aqueous solution might be the ACE mechanism.[51] In addition, the LUMO energy levels of OFX and FO were −0.30 eV (ref. 33) and −1.45 eV, which are higher than the LUMO of H₄BTDI (−3.35 eV) (Fig. 9). Therefore, the excited electrons of the LUMO of OFX and FO were transferred to the LUMO of the H₄BTDI of **JXUST-12a**, which made **JXUST-12a** display fluorescence turn-on effect and blue shift.[46,47,53,54] Therefore, the detection of OFX and FO by **JXUST-12a** in the aqueous solution might be attributed to the ACE and PET mechanisms.

Conclusions

One novel Tb[III]-based MOF (**JXUST-12**) have been successfully designed and synthesized by the incorporation of Tb[III] ions and H₄BTDI ligands under solvothermal conditions. Interestingly, the temperature- and solvent-induced reversible SCSC conversion between **JXUST-12** and **JXUST-12a** could be achieved and the transformed **JXUST-12a** exhibits excellent water stability and pH stabilities. **JXUST-12** and **JXUST-12a** exhibit the fluorescence turn-off effect toward NFT, NZF and DCN in EtOH solution. Besides, **JXUST-12a** not only has the fluorescence turn-off effect toward NFT and NZF, but also has a fluorescence turn-on effect and blue shift toward OFX and FO in the aqueous solution. The LODs of **JXUST-12a** for the detection of NFT, NZF or DCN were lower than those of **JXUST-12**, indicating better fluorescence sensing properties. The fluorescence test papers and composite films were further developed and the practical application of fluorescence sensors was expanded. Further studies of MOF-based fluorescent sensors with SCSC transformation are under way in our group.

Conflicts of interest

There are no conflicts to declare.

Acknowledgements

1510 | *Inorg. Chem. Front.*, 2022, **9**, 1504–1513

This journal is © the Partner Organisations 2022

Notes and references

1 A. Mallick, A. M. El-Zohry, O. Shekhah, J. Yin, J.-T. Jia, H. Aggarwal, A.-H. Emwas, O. F. Mohammed and M. Eddaoudi, Unprecedented ultralow detection limit of amines using a thiadiazole-functionalized Zr(IV)-based metal-organic framework, *J. Am. Chem. Soc.*, 2019, **141**, 7245–7249.

2 D.-X. Gu, W.-T. Yang, D.-Y. Lin, X.-D. Qin, Y.-H. Yang, F.-X. Wang, Q.-H. Pan and Z.-M. Su, Water-stable lanthanide-based metal-organic gel for the detection of organic amines and white-light emission, *J. Mater. Chem. C*, 2020, **8**, 13648–13654.

3 J.-K. Jin, K. Wu, X.-Y. Liu, G.-Q. Huang, Y.-L. Huang, D. Luo, M. Xie, Y.-F. Zhao, W.-G. Lu, X.-P. Zhou, J. He and D. Li, Building a pyrazole–benzothiadiazole–pyrazole photosensitizer into metal-organic frameworks for photocatalytic aerobic oxidation, *J. Am. Chem. Soc.*, 2021, **143**, 21340–21349.

4 S.-J. Liu, C. Cao, S.-L. Yao, T.-F. Zheng, Z.-X. Wang, C. Liu, J.-S. Liao, J.-L. Chen, Y.-W. Li and H.-R. Wen, Temperature- and vapor-induced reversible single-crystal-to-single-crystal transformations of three 2D/3D Gd^{III}-organic frameworks exhibiting significant magnetocaloric effects, *Dalton Trans.*, 2017, **46**, 64–70.

5 R. Li, S.-H. Wang, X.-X. Chen, J. Lu, Z.-H. Fu, Y. Li, G. Xu, F.-K. Zheng and G.-C. Guo, Highly anisotropic and water molecule-dependent proton conductivity in a 2D homochiral copper(II) metal–organic framework, *Chem. Mater.*, 2017, **29**, 2321–2331.

6 J. Wang, Y. Zhang, P.-X. Zhang, J.-B. Hu, R.-B. Lin, Q. Deng, Z.-L. Zeng, H.-B. Xing, S.-G. Deng and B.-L. Chen, Optimizing pore space for flexible-robust metal–organic framework to boost trace acetylene removal, *J. Am. Chem. Soc.*, 2020, **142**, 9744–9751.

7 C. Wang, L.-J. Li, J. G. Bell, X.-X. Lv, S.-F. Tang, X.-B. Zhao and K. M. Thomas, Hysteretic gas and vapor sorption in flexible interpenetrated lanthanide-based metal-organic frameworks with coordinated molecular gating via reversible single-crystal-to-single-crystal transformation for enhanced selectivity, *Chem. Mater.*, 2015, **27**, 1502–1516.

8 Z.-J. Li, M. Lei, H.-L. Bao, Y. Ju, H.-J. Lu, Y.-X. Li, Z.-H. Zhang, X.-F. Guo, Y. Qian, M.-Y. He, J.-Q. Wang, W. Liu and J. Lin, A cationic thorium-organic framework with triple single-crystal-to-single-crystal transformation peculiarities for ultrasensitive anion recognition, *Chem. Sci.*, 2021, **12**, 15833–15842.

9 A. Atilgan, T. Islamoglu, A. J. Howarth, J. T. Hupp and O. K. Farha, Detoxification of a sulfur mustard simulant using a BODIPY-functionalized zirconium-based metal-organic framework, *ACS Appl. Mater. Interfaces*, 2017, **9**, 24555–24560.

10 Z.-Q. Yao, J. Xu, B. Zou, Z.-P. Hu, K. Wang, Y.-J. Yuan, Y.-P. Chen, R. Feng, J.-B. Xiong, J.-L. Hao and X.-H. Bu, A dual-stimuli-responsive coordination network featuring a reversible wide-range luminescence tuning behavior, *Angew. Chem., Int. Ed.*, 2019, **58**, 5614–5618.

11 W.-W. He, S.-L. Li and Y.-Q. Lan, Liquid-free single-crystal to single-crystal transformations in coordination polymers, *Inorg. Chem. Front.*, 2018, **5**, 279–300.

12 Y.-Q. Lan, H.-L. Jiang, S.-L. Li and Q. Xu, Solvent-Induced controllable synthesis, single-crystal to single-crystal transformation and encapsulation of Alq3 for modulated luminescence in (4,8)-connected metal-organic frameworks, *Inorg. Chem.*, 2012, **51**, 7484–7491.

13 X.-J. Hong, M.-F. Wang, H.-G. Jin, Q.-G. Zhan, Y.-T. Liu, H.-Y. Jia, X. Liu and Y.-P. Cai, Single-crystal to single-crystal transformation from a 1-D chain-like structure to a 2-D coordination polymer on heating, *CrystEngComm*, 2013, **15**, 5606–5611.

14 J. Yang, X.-Q. Wang, F.-N. Dai, L.-L. Zhang, R.-M. Wang and D.-F. Sun, Improving the porosity and catalytic capacity of a zinc paddlewheel metal-organic framework (MOF) through metal-ion metathesis in a single-crystal-to-single-crystal fashion, *Inorg. Chem.*, 2014, **53**, 10649–10653.

15 Y.-H. Yang, G.-J. Ren, W.-K. Yang, D.-Y. Lin, M.-L. Li, Z. Chang, Y. Fang, Z.-Q. Liang and Q.-H. Pan, Single-crystal to single-crystal transformation of metal-organic framework nanoparticles for encapsulation and pH-stimulated release of camptothecin, *ACS Appl. Nano Mater.*, 2021, **4**, 7191–7198.

16 S.-S. Bao, N.-Z. Li, J. M. Taylor, Y. Shen, H. Kitagawa and L.-M. Zheng, Co-Ca phosphonate showing humidity-sensitive single crystal to single crystal structural transformation and tunable proton conduction properties, *Chem. Mater.*, 2015, **27**, 8116–8125.

17 N. Li, J. Xu, R. Feng, T.-L. Hu and X.-H. Bu, Governing metal-organic frameworks towards high stability, *Chem. Commun.*, 2016, **52**, 8501–8513.

18 F.-F. Li, L. Zhang, L.-L. Gong, C.-S. Yan, H.-Y. Gao and F. Luo, Reversible photo/thermoswitchable dual-color fluorescence through single-crystal-to-single-crystal transformation, *Dalton Trans.*, 2017, **46**, 338–341.

19 J. Jin, J.-J. Xue, Y.-C. Liu, G.-P. Yang and Y.-Y. Wang, Recent progresses in luminescent metal-organic frameworks (LMOFs) as sensors for the detection of anions and cations in aqueous solution, *Dalton Trans.*, 2021, **50**, 1950–1972.

20 L. Ding, Y. Zhao, H. Li, Q. Zhang, W. Yang, B. Fu and Q. Pan, A highly selective ratiometric fluorescent probe for doxycycline based on the fluorescence sensitization effect of bovine serum albumin, *J. Hazard. Mater.*, 2021, **416**, 125759.

21 M.-L. Li, G.-J. Ren, W.-T. Yang, Y.-H. Yang, W.-K. Yang, Y. Gao, P.-F. Qiu and Q.-H. Pan, Dual-emitting piezofluorochromic dye@MOF for white-light generation, *Chem. Commun.*, 2021, **57**, 1340–1343.

22 J. Cheng, Y.-F. Li, J. Zhong, Z.-W. Lu, G.-T. Wang, M.-M. Sun, Y.-Y. Jiang, P. Zou, X.-X. Wang, Q.-B. Zhao, Y.-Y. Wang and H.-B. Rao, Molecularly imprinted electrochemical sensor based on biomass carbon decorated with MOF-derived Cr_2O_3 and silver nanoparticles for selective

This journal is © the Partner Organisations 2022

Inorg. Chem. Front., 2022, **9**, 1504–1513 | **1511**

and sensitive detection of nitrofurazone, *Chem. Eng. J.*, 2020, **398**, 125664.

23 H.-W. Yang, P. Xu, B. Ding, Z.-Y. Liu, X.-J. Zhao and E.-C. Yang, A highly-stable luminescent Eu-MOF exhibiting efficient response to nitrofuran antibiotics through inner filter effect and photoinduced electron transfer, *Eur. J. Inorg. Chem.*, 2019, **2019**, 5077–5084.

24 A. S. Oberoi, Y.-Y. Jia, H.-Q. Zhang, S. K. Khanal and H. Lu, Insights into the fate and removal of antibiotics in engineered biological treatment systems: a critical review, *Environ. Sci. Technol.*, 2019, **53**, 7234–7264.

25 P.-L. Wang, L.-H. Xie, E. A. Joseph, J.-R. Li, X.-O. Su and H.-C. Zhou, Metal-organic frameworks for food safety, *Chem. Rev.*, 2019, **119**, 10638–10690.

26 Y.-F. Xie, X.-Y. Zhu, Y.-Y. Sun, H.-Y. Wang, H. Qian and W.-R. Yao, Rapid detection method for nitrofuran antibiotic residues by surface-enhanced raman spectroscopy, *Eur. Food Res. Technol.*, 2012, **235**, 555–561.

27 G. Chakraborty, P. Das and S. K. Mandal, Strategic construction of highly stable metal-organic frameworks combining both semi-rigid tetrapodal and rigid ditopic linkers: selective and ultrafast sensing of 4-nitroaniline in water, *ACS Appl. Mater. Interfaces*, 2018, **10**, 42406–42416.

28 B. Wang, X.-L. Lv, D.-W. Feng, L.-H. Xie, J. Zhang, M. Li, Y.-B. Xie, J.-R. Li and H.-C. Zhou, Highly stable Zr(IV)-based metal-organic frameworks for the detection and removal of antibiotics and organic explosives in water, *J. Am. Chem. Soc.*, 2016, **138**, 6204–6216.

29 N. Seal, M. Singh, S. Das, R. Goswami, B. Pathak and S. Neogi, Dual-functionalization actuated trimodal attribute in ultra-robust MOF: exceptionally selective capture and effectual fixation of CO_2 with fast-responsive, nanomolar detection of assorted organo-contaminants in water, *Mater. Chem. Front.*, 2021, **5**, 979–994.

30 C.-L. Tao, B. Chen, X.-G. Liu, L.-J. Zhou, X.-L. Zhu, J. Cao, Z.-G. Gu, Z.-J. Zhao, L. Shen and B.-Z. Tang, A highly luminescent entangled metal-organic framework based on pyridine-substituted tetraphenylethene for efficient pesticide detection, *Chem. Commun.*, 2017, **53**, 9975–9978.

31 M. Hollweg, H.-P. Kapfhammer, M. Krupinski and H.-J. Möller Nervenarzt, Psychopathol ogische syndrome unter behandlung mit gyrasehemmern, *Nervenarzt*, 1997, **68**, 38–47.

32 J.-N. Xiao, M.-Y. Liu, F.-L. Tian and Z.-L. Liu, Stable Europium-based metal-organic frameworks for naked-eye ultrasensitive detecting fluoroquinolones antibiotics, *Inorg. Chem.*, 2021, **60**, 5282–5289.

33 C.-P. Li, W.-W. Long, Z. Lei, L. Guo, M.-J. Xie, J. Lü and X.-D. Zhu, Anionic metal-organic framework as a unique turn-on fluorescent chemical sensor for ultra-sensitive detection of antibiotics, *Chem. Commun.*, 2020, **56**, 12403–12406.

34 R. A. Pearson, C. Evans and J. G. Bendall, Nitrofurazone quantification in milk at the european union minimum required performance limit of 1 ng g^{-1}: circumventing the semicarbazide problem, *Food Addit. Contam., Part A*, 2016, **33**, 1324–1336.

35 M. Tubino, M. M. D. C. Vila and M. N. Palumbo, Determination of nitrofurazone in topical pharmaceutical preparations: comparison of the UV-visible diffuse reflectance versus transmittance versus HPLC methods, *J. Braz. Chem. Soc.*, 2009, **20**, 1901–1907.

36 S.-L. Yao, S.-J. Liu, X.-M. Tian, T.-F. Zheng, C. Cao, C.-Y. Niu, Y.-Q. Chen, J.-L. Chen, H.-P. Huang and H.-R. Wen, A Zn^{II}-based metal-organic framework with a rare *tcj* topology as a turn-on fluorescent sensor for acetylacetone, *Inorg. Chem.*, 2019, **58**, 3578–3581.

37 J. Li, S.-L. Yao, S.-J. Liu and Y.-Q. Chen, Fluorescent sensors for aldehydes based on luminescent metal-organic frameworks, *Dalton Trans.*, 2021, **50**, 7166–7175.

38 Z. Lei, L. Hu, Z.-H. Yu, Q.-Y. Yao, X. Chen, H. Li, R.-M. Liu, C.-P. Li and X.-D. Zhu, Ancillary ligand enabled structural and fluorescence diversity in metal-organic frameworks: application for the ultra-sensitive detection of nitrofuran antibiotics, *Inorg. Chem. Front.*, 2021, **8**, 1290–1296.

39 Q. Cheng, X. Han, Y. Tong, C. Huang, J. Ding and H.-W. Hou, Two 3D Cd(II) metal–organic frameworks linked by benzothiadiazole dicarboxylates: fantastic S@Cd_6 cage, benzothiadiazole antidimmer, and dual emission, *Inorg. Chem.*, 2017, **56**, 1696–1705.

40 W.-Q. Zhang, Q.-Y. Li, J.-Y. Cheng, K. Cheng, X.-Y. Yang, Y.-W. Li, X.-S. Zhao and X.-J. Wang, Ratiometric luminescent detection of organic amines due to the induced lactam–lactim tautomerization of organic linker in a metal-organic framework, *ACS Appl. Mater. Interfaces*, 2017, **9**, 31352–31356.

41 A. M. El-Zohry, A. Alturki, J. Yin, A. Mallick, O. Shekhah, M. Eddaoudi, B. S. Ooi and O. F. Mohammed, Tunable twisting motion of organic linkers via concentration and hydrogen-bond formation, *J. Phys. Chem. C*, 2019, **123**, 5900–5906.

42 X.-M. Tian, S.-L. Yao, C.-Q. Qiu, T.-F. Zheng, Y.-Q. Chen, H.-P. Huang, J.-L. Chen, S.-J. Liu and H.-R. Wen, Turn-on luminescent sensor toward Fe^{3+}, Cr^{3+}, and Al^{3+} based on a Co(II) metal-organic framework with open functional sites, *Inorg. Chem.*, 2020, **59**, 2803–2810.

43 M. Llunell, D. Casanova, J. Cirera, P. Alemany and S. Alvarez, *SHAPE, version 2.1*, Universitat de Barcelona, Barcelona, Spain, 2013.

44 D. Zhao, D. Yue, K. Jiang, Y.-J. Cui, Q. Zhang, Y. Yang and G.-D. Qian, Ratiometric dual-emitting MOF ⊃ dye thermometers with a tunable operating range and sensitivity, *J. Mater. Chem. C*, 2017, **5**, 1607–1613.

45 C.-L. Song, Y.-B. He, B. Li, Y.-J. Ling, H.-L. Wang, Y.-L. Feng, R. Krishnac and B.-L. Chen, Enhanced CO_2 sorption and selectivity by functionalization of a NbO-type metal-organic framework with polarized benzothiadiazole moieties, *Chem. Commun.*, 2014, **50**, 12105–12108.

46 S. Pramanik, C. Zheng, X. Zhang, T. J. Emge and J. Li, New microporous metal-organic framework demonstrating unique selectivity for detection of high explosives and aromatic compounds, *J. Am. Chem. Soc.*, 2011, **133**, 4153–4155.

47 Z.-Q. Liu, Y. Zhao, X.-D. Zhang, Y.-S. Kang, Q.-Y. Lu, M. Azam, S. I. Al-Resayes and W.-Y. Sun, Metal-organic

1512 | *Inorg. Chem. Front.*, 2022, **9**, 1504–1513

This journal is © the Partner Organisations 2022

frameworks with 1,4-di(1H-imidazol-4-yl)benzene and varied carboxylate ligands for selectively sensing Fe(III) ion and ketone molecules, *Dalton Trans.*, 2017, **46**, 13943–13951.

48 Y.-F. Zhao, M.-Y. Wan, J.-P. Bai, H. Zeng, W.-G. Lu and D. Li, pH-Modulated luminescence switching in a Eu-MOF: rapid detection of acidic amino acids, *J. Mater. Chem. A*, 2019, **7**, 11127–11133.

49 M. Wang, L. Guo and D.-P. Cao, Metal-organic framework as luminescence turn-on sensor for selective detection of metal ions: absorbance caused enhancement mechanism, *Sens. Actuators, B*, 2018, **256**, 839–845.

50 W. Chen, R.-Q. Fan, J.-Z. Fan, H.-Y. Liu, T.-C. Sun, P. Wang and Y.-L. Yang, Lanthanide coordination polymer-based composite films for selective and highly sensitive detection of $Cr_2O_7^{2-}$ in aqueous media, *Inorg. Chem.*, 2019, **58**, 15118–15125.

51 S.-Y. Wu, M.-C. Zhu, Y. Zhang, M. Kosinova, V. P. Fedin and E. Gao, A water stable lanthanide coordination polymer as multicenter platform for ratiometric luminescent sensing antibiotics, *Chem. – Eur. J.*, 2020, **26**, 3137–3144.

52 X.-H. Wang, M.-Y. Lei, T.-J. Zhang, Q.-F. Zhang, R.-F. Zhang and M. Yang, A water-stable multi-responsive luminescent Zn-MOF sensor for detecting of TNP, NZF and $Cr_2O_7^{2-}$ in aqueous media, *Dalton Trans.*, 2021, **50**, 3816–3824.

53 S. S. Nagarkar, B. Joarder, A. K. Chaudhari, S. Mukherjee and S. K. Ghosh, Highly selective detection of nitro explosives by a luminescent metal-organic framework, *Angew. Chem., Int. Ed.*, 2013, **52**, 2881–2885.

54 S.-Y. Wu, Y.-N. Lin, J.-W. Liu, W. Shi, G.-M. Yang and P. Cheng, Rapid detection of the biomarkers for carcinoid tumors by a water stable luminescent lanthanide metal-organic framework sensor, *Adv. Funct. Mater.*, 2018, **28**, 1707169.

55 W. P. Lustig, S. Mukherjee, N. D. Rudd, A. V. Desai, J. Li and S. K. Ghosh, Metal-organic frameworks: functional luminescent and photonic materials for sensing applications, *Chem. Soc. Rev.*, 2017, **46**, 3242–3285.

This journal is © the Partner Organisations 2022

Inorg. Chem. Front., 2022, **9**, 1504–1513 | **1513**